



N, O-dual coordination regulation directs the design of active sites on nanoclusters for highly efficient catalytic water purification

Fangfang Dai^a, Mingsen Xie^a, Shuoxuan Wang^a, Weiqiang Lv^c, Yong Wang^a, Zhen Zhang^{a,*}, Xiaoquan Lu^{b,**}

^a Tianjin Key Laboratory of Molecular Optoelectronic Sciences, Department of Chemistry, School of Science, Tianjin University, Tianjin 300072, PR China

^b Key Laboratory of Bioelectrochemistry and Environmental Analysis of Gansu Province, College of Chemistry and Chemical Engineering, Northwest Normal University, Lanzhou 730070, PR China

^c Yangtze Delta Region Institute (Huzhou), School of Physics, University of Electronic Science and Technology of China, Huzhou 313001, PR China

ARTICLE INFO

Keywords:

N, O-double doping
Nanoclusters catalysts
Advanced oxidation processes
Organic pollutant degradation
Antibacterial

ABSTRACT

Advanced oxidation processes (AOPs) are regarded as promising strategies for generating powerful oxygen-containing radicals that can degrade nearly all organic compounds. However, developing catalysts with highly active sites for carrying out AOPs is still a significant challenge. Herein, we design and synthesize of ultra-small cobalt nanoclusters with N, O-dual coordination (O-Co-N) on porous carbonized peat moss (CPM-Co-2) for the efficient catalytic purification of water through peroxymonosulfate (PMS)-based AOPs. Density functional theory calculations revealed that introducing O causes the *d*-band center of the O-Co-N configuration to shift away from the Fermi level, which significantly decreased the desorption energy of sulfate radicals ($\text{SO}_4^{\cdot-}$) and accelerated the rate-limiting step to promote the reaction. The CPM-Co-2 showed excellent catalytic activity and stability in the remediation of organic pollutants and bacteria. The immensely increased catalytic activity achieved through regulating the metal coordination environment provided useful insights for the future design and synthesis of catalyst.

1. Introduction

With the rapid growth of industrialization and civilization, water resources are facing severe deterioration, with persistent organic pollutants (POPs) and bacteria posing a threat to human health [1–3]. Various methods [4], such as adsorption [5,6], chlorination [7,8], ozone oxidation [9,10], and ultraviolet irradiation [11], have been developed to treat contaminated water. Among them, peroxymonosulfate (PMS)-based advanced oxidation processes (AOPs) have gained considerable attention because they generate highly active reactive oxygen species (ROS) that can degrade various organic compounds in water owing to their powerful oxidizing capability [12–14]. Heterogeneously supported ultra-small transition metal nanocluster-based catalysts have emerged as new research frontiers for various catalytic reactions, such as AOPs, owing to their ease of separation and stability [15–17]. On the one hand, dispersed metal nanoclusters expose more reactive centers owing to their high atomic utilization [18]. On the other

hand, the interactions between the nanoclusters and the support materials can modulate the local electronic structure of the metal centers, thereby improving electron transfer and enhancing the activity of each active site. The challenge is how to rationally coordinate metal nanoclusters on the support to construct efficient active sites for improving the activity of catalysts for the activation of PMS.

Carbon materials with large specific surface areas, easy modification, and environmental friendliness are regarded as promising supports in heterogeneous catalysis [19–21]. In particular, doping carbon materials with heteroatoms (such as N, S, or O) can modulate the coordination environment of the anchored metal, thereby regulating the charge transfer between the anchored metal species and the carbon support to a different degree, as well as improving the catalytic performance [22–26]. For example, Liu et al. reported that the anchoring Co atoms on N-doped carbon substrates form CoN_4 , which acted as the active center by significantly accelerating the degradation of bisphenol A (BPA) [27]. Zhao et al. selected nitrogen-free lignin with oxygen-rich functional

* Corresponding author.

** Correspondence to: Environmental Analysis of Gansu Province, College of Chemistry and Chemical Engineering, Northwest Normal University, Lanzhou 730070, P. R. China.

E-mail addresses: zhzhen@tju.edu.cn (Z. Zhang), luxq@nwnu.edu.cn (X. Lu).

<https://doi.org/10.1016/j.apcatb.2023.122510>

Received 29 November 2022; Received in revised form 14 January 2023; Accepted 20 February 2023

Available online 21 February 2023

0926-3373/© 2023 Elsevier B.V. All rights reserved.

groups as a carbon support to form metal-oxygen coordination bonds ($M-O_x$), which exhibited dramatically enhanced catalytic activity [28]. These studies demonstrate the unique advantages of carbon materials as catalyst supports and the crucial role of the active site configuration on the catalytic performance. Although satisfactory success has been achieved, exploring other types of metal coordination systems may synergistically improve the stability of the supported metal and regulate the electrons on the metal to improve its catalytic performance, giving it a prominent advantage for carrying out AOPs.

The key points to apply AOPs in practical applications can be attributed to two aspects, the catalysts with high catalytic reaction performance and that can be easily and rapidly synthesized on a large scale with controllable quality [29–31]. Calcining biomass with abundant heteroatoms to large-scale carbon-supported catalysts is a feasible strategy [32]. The naturally existing abundant and uniformly distributed functional groups (e.g., N- and O-containing groups) in biomass-based precursors can readily anchor and reduce impregnated metal ions on the carbon supports by generating new coordination configurations [33–35]. Therefore, it is highly desirable to systematically explore the newly introduced catalytically active configurations of biocarbon-supported catalysts, which would potentially pave the way for their design and wide practical applications.

Herein, we report the design and synthesis of ultra-small cobalt nanoclusters (CoNCs) with N, O-dual coordination (O-Co-N) on porous carbonized peat moss (CPM-Co-2) as a highly active and stable catalyst for the efficient degradation of POPs and antibacterial activity by activating PMS in wastewater. The catalyst was synthesized via the facile pyrolysis of peat moss, and its internal N- and O-rich functional groups could effectively anchor and further regulate the electronic structure of CoNCs. Both the experiments and density functional theory (DFT) calculations confirmed that the O-Co-N coordination could greatly enhance the catalytic performance owing to the lowering of the energy barrier for the desorption of $SO_4^{\cdot-}$, which is the rate-limiting step of PMS activation. The CPM-Co-2 catalysts exhibited excellent catalytic activity with the modified kinetic model (k -value) as high as 116.5, 25.9, and 28.63 $\mu\text{mol s}^{-1} \text{g}^{-1}$ for rhodamine B (RhB), BPA, and 2,4-dichlorophenol (2,4-DCP), respectively. Additionally, different microorganisms, including *Escherichia coli* (*E. coli*) and *Staphylococcus aureus* (*S. aureus*), can be almost completely killed within 15 min under the CPM-Co-2/PMS system. Therefore, our study provides a strategy for improving catalytic performance through the regulation of the coordination environment, thereby achieving effective and sustainable remediation of organic pollutants and bacteria in water resources.

2. Materials and methods

2.1. Pretreatment of peat moss leaves (PM)

Peat moss is readily available in Shaoxing, Zhejiang Province. According to the previous literatures, the impurities in the peat moss were completely removed, leaving only small and intact peat moss leaves (PM), and washed several times with distilled water for subsequent use.

2.2. Preparation of carbonized peat moss leaves-cobalt nanocluster catalyst (CPM-Co)

0.5 g of pretreated PM were transferred to a 250 mL round bottom flask, and then added 2 mM, 4 mM, 6 mM, and 8 mM $\text{Co}(\text{NO}_3)_2 \cdot 6 \text{H}_2\text{O}$ solutions, respectively. The leaves were fully immersed in solution and refluxed at 80 °C for 3 h under vigorous stirring. After the reaction solution was cooled to room temperature, the PM were turned into a pink purple product was taken out from the flask, and then vacuum dried in an oven at 50 °C overnight. The obtained precursor was placed in a tube furnace, calcined at 250 °C for 4 h in a nitrogen atmosphere for pretreatment, and the heating rate was 5 °C $\cdot\text{min}^{-1}$. The carbon black material collected from the furnace was further carbonized in a tube

furnace under a flowing nitrogen atmosphere at a high temperature of 900 °C for 3 h, and the temperature increase rate was 3 °C $\cdot\text{min}^{-1}$. The resulting N, O-double doped porous carbon catalysts are labeled CPM-Co-1, CPM-Co-2, CPM-Co-3, and CPM-Co-4, respectively. Unless otherwise specified, the catalyst (CPM-Co-2) discussed below were synthesized with 4 mM $\text{Co}(\text{NO}_3)_2 \cdot 6 \text{H}_2\text{O}$ solution.

2.3. Preparation of carbonized peat moss catalyst (CPM)

For comparative experiments, the carbonized peat moss catalyst was prepared in the same way. 1 g of pretreated peat moss leaves were placed in a tube furnace, calcined at 250 °C for 4 h in a nitrogen atmosphere, and the heating rate was 5 °C $\cdot\text{min}^{-1}$. The carbon black material collected from the furnace was further carbonized in a tube furnace under a flowing nitrogen atmosphere at a high temperature of 900 °C for 3 h, with a temperature increase rate of 3 °C $\cdot\text{min}^{-1}$, and the resulting sample was labeled CPM.

2.4. Characterizations

The morphology and particle size of the nanoclusters were characterized by transmission electron microscopy (TEM, JEOL-2100 F, Japan) and scanning electron microscopy (SEM, SU8010, Hitachi, Japan). High-resolution transmission electron microscope (HRTEM) images, elemental mapping and energy-dispersive spectrometry (EDS) were performed on a JEM-3010. The element valence states were conducted by the X-ray photoelectron spectroscopy (XPS, ESCALAB 250Xi, Japan). X-ray powder diffraction (XRD) was collected on X-ray diffraction instrument (RIGAKU SMARTLAB9KW, Japan). Inductively coupled plasma mass spectrometry (ICP-MS, Agilent 7700x, USA) was used to determine the content of Co in catalysts. Ultraviolet–visible (UV–vis) absorption spectra were collected on a UV–visible spectrophotometer (UV-3600Plus). The electron paramagnetic resonance (EPR) spectra were collected on a JES-FA200 spectrometer with a center field at 3320 G and a sweep width of 140 G at room temperature. The Raman spectra were characterized by the confocal microprobe Raman system (DXR2xi). The Brunauer–Emmett–Teller (BET) surface area and porous structure were measured by nitrogen adsorption and desorption (N_2 adsorption-desorption) at 77 K using a Bel Japan Inc. model BELSOPR-max analyzer and the samples were degassed at 250 °C for 8 h under vacuum (10^{-5} bar) before analysis. The intermediates of the pollutants were investigated by liquid chromatography-tandem mass spectrometry (LC-MS, Sciex 6500plus QTRAP, America). The total organic carbon content of the system was measured by total organic carbon analyzer (TOC-L, Shimadzu, Japan) to quantify the mineralization degree of pollutant.

2.5. Catalytic activity

The catalyst degradation performance was conducted at 25 °C in a 20 mL reactor containing 200 mg/L RhB as an initial solution. In a typical experiment, 4 mg of catalyst was added into 20 mL of RhB solution and stirred for 5 min to establish the adsorption desorption equilibrium. The reaction was initiated by adding 0.2 g/L of PMS aqueous solution. At different time points, 1 mL of the reaction solution was withdrawn and immediately quenched with 0.1 mL of methanol solution. For the cycling test, the catalyst was recycled after each run of the experiment by filtration and washed thoroughly with copious amounts of deionized water. Since the initial concentration of RhB was too high and exceeded the UV–vis test range, each group of samples were diluted seven times. The concentration of RhB was analyzed by ultraviolet spectrometer at 554 nm wavelength.

The concentration of BPA and 2,4-DCP were analyzed by high performance liquid chromatography (HPLC, Agilent, 1260) at the detection wavelength of 225 nm and 280 nm with a methanol/water mixture (70:30, v/v) as the mobile phase. The concentrations of leached cobalt were quantified by ICP-MS. The reaction rate was evaluated by a pseudo

first-order kinetics model (Eq. (1)), and the RhB adsorption efficiency (R %) was calculated using Eq. (2):

$$\ln(C_0/C_t) = kt \quad (1)$$

$$R\% = 100 \times (C_0 - C_e)/C_0 \quad (2)$$

where C_0 is the initial pollutant concentration, C_t is the concentration at a certain time t during the degradation process, C_e is the concentration of adsorbate at equilibrium, and k is the reaction rate constant.

2.6. A modified kinetic model (k -value)

Dividing the degradation reaction rate of organic pollutants by catalyst concentration (C_{cat}) and then by multiplying organic pollutant concentration (C_{org}) to obtain the improved kinetic model (k -value) ($\mu\text{mol s}^{-1} \text{g}^{-1}$).

$$k\text{-value} = \frac{K \times C_{org}}{C_{cat}} \quad (3)$$

where C_{cat} is the concentration of catalyst (g/L), K is the reaction rate of organic contaminant (min^{-1}), and C_{org} ($\mu\text{mol/L}$) is the concentration of the organic contaminant.

2.7. Antibacterial experiments

S. aureus and *E. coli* as the typical Gram-positive bacteria and Gram-negative bacteria were cultured in liquid medium, respectively. The bacterial solutions were incubated in a shaker at 200 rpm for 12 h with a constant temperature of 37 °C. After incubation, the collected bacteria were washed three times by centrifugation with PBS (10 mM, pH = 7.4). The collected bacteria were diluted to 10^7 CFU mL^{-1} and divided into four groups: PBS, PMS, CPM-Co-2, CPM-Co-2 + PMS (PMS = 0.1 M, CPM-Co-2 = 0.2 g/L). After 20 min, 10 μL of the different mixtures were spread evenly on agar plates and transferred to an incubator at 37 °C for overnight incubation. Finally, the bacterial survival rate was determined

by the plate counting method. All experiments were repeated three times in parallel.

3. Results and discussion

3.1. Theoretical prediction of DFT calculation

To rationally design high-performance catalysts, DFT calculations were performed to investigate whether the introduction of O to form a new N, O-dual coordination would promote the activation of PMS. First, we constructed two models of Co-N and O-Co-N based on graphene to calculate the differential charge density (Figs. 1a, b, S1, and S4). By comparison, it can be seen that in the O-Co-N model, electrons are transferred from Co to the adjacent O atom on the carbon support, causing the Co to be in an electron-deficient state, that is, Co^{2+} and/or Co^{3+} , which is ideal for activating PMS [36,37]. Considering the two constructed models, PMS is preferentially adsorbed on the surface of the cobalt cluster, and there is no clear gain or loss of electrons on O but the electron density on the cobalt cluster decreases, which shows that cobalt is the active site (Figs. 4, S2, and S5). When compared with the differential density map of Co-N, the O-Co-N model shows greater electron transfer in the adsorption steps of PMS and radicals, indicating that the activity of Co-N increases due to the introduction of O (Figs. S3 and S6). To further explore the influence of the introduced O in the catalytic decomposition of PMS, the change in the Gibbs free energy (ΔG) of the reaction was determined by considering the reaction steps shown in Fig. 1c. The formation of HSO_5^* and SO_4^* are both exothermic processes, indicating that the adsorption and decomposition of PMS are spontaneous. More importantly, the desorption of SO_4^* is the rate-limiting step on both active sites [38,39]. The desorption energy of SO_4^* on the surface of O-Co-N is smaller than that of Co-N, which accelerates the rate-limiting step. To further understand the changes caused by the coordination of nitrogen and oxygen, we analyzed the d -band center of the material, which plays a crucial role in the catalytic process. In Fig. 1d, the introduction of O causes the d -band center of CoNCs to shift away from the Fermi level, thereby weakening the adsorption capacity

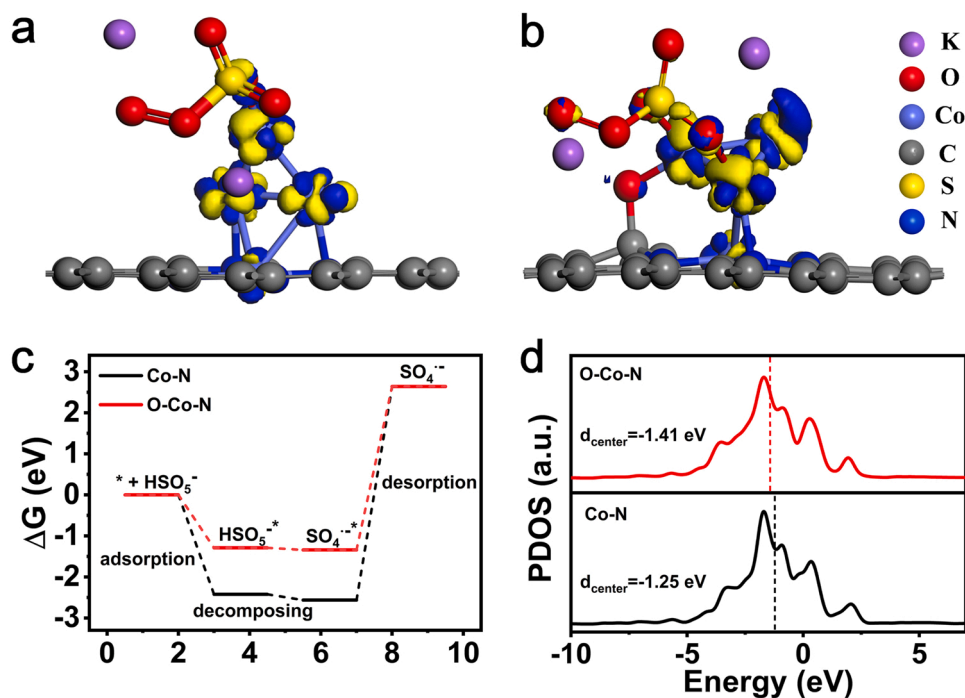


Fig. 1. The charge density difference on a) Co-N, and b) O-Co-N under the adsorption of PMS. c) Calculated free energy profile for PMS to SO_4^{2-} process on Co-N and O-Co-N. d) d -band center of Co on Co-N and O-Co-N. The adsorption site is denoted by an asterisk (*). Electron excess and deficiency are represented as blue and yellow isosurfaces, respectively.

of the adsorbed species, which may be key in decreasing the desorption energy barrier. Improving the desorption capacity of $\text{SO}_4^{\bullet-}$ is beneficial for the subsequent step and accelerates the degradation of pollutants. We also constructed a DFT calculation model containing 13 Co atoms to replace the Co nanoclusters (Figs. S7–S14), and the results were consistent with those of the constructed four Co atoms nanoclusters (Fig. 1). In conclusion, based on the theoretical evaluation conducted, the new active site formed via N, O-dual coordination can rapidly activate PMS, and its high catalytic activity will be further demonstrated in the degradation of organic pollutants and antibacterial experiments.

3.2. Synthesis and characterization of CPM-Co-2 catalyst

To fabricate N, O-dual-doped three-dimensional (3D) porous biocarbon-supported metal nanocluster catalysts, natural peat moss leaves (PM) were immersed in the Co precursor solution, followed by simple activation and high-temperature calcination (Scheme 1). The catalysts were labeled as CPM-Co-1, CPM-Co-2, CPM-Co-3, and CPM-Co-4, respectively. The morphologies of CPM-Co-2 were characterized using scanning electron microscopy (SEM) and transmission electron microscopy (TEM). The SEM images show a silkworm-/worm-like microstructure of the PM (Fig. S15). The CPM-Co-2 catalyst maintains its original unique porous 3D structure without collapse of the carbon framework (Figs. 2a and S16). Because of the large number of open microchannels in the PM, the $\text{Co}(\text{NO}_3)_2$ precursor solution can permeate into the whole leaves, forming uniformly dispersed Co nanoclusters with an average particle size of 2 nm, as shown in the TEM image in Fig. 2b. As shown in the high-resolution TEM (HRTEM) image, the lattice spacing of CoNCs is 0.20 nm, corresponding to the (1 1 1) plane of metallic cobalt (Fig. 2c) [40]. Multiple TEM tests in randomly selected regions showed the homogeneous CPM-Co-2 catalysts verified the consistency of the catalysts (Fig. S17). To verify the distribution of each element on the surface of CPM-Co-2, energy-dispersive X-ray spectroscopy (EDX) and energy dispersive X-ray spectroscopy (EDS) element mappings were performed. As displayed in Figs. 2d–h and S18, CPM-Co-2 contains C, N, O, and Co species that are uniformly distributed on the surface of the carbonized peat moss leaves (CPM). As a biocarbon substrate, the X-ray diffraction (XRD) patterns of CPM reflect the (0 0 2) and (1 0 0) crystal planes of graphitic carbon at 23.0° and 43.7° (Fig. S19), respectively. After successful loading of metallic cobalt, the XRD patterns of the both catalysts display the reflections for the (1 1 1), (2 0 0) and (2 2 0) crystal planes corresponded to the metal Co (JCPDS No 15–0806) (Fig. 2i) [41].

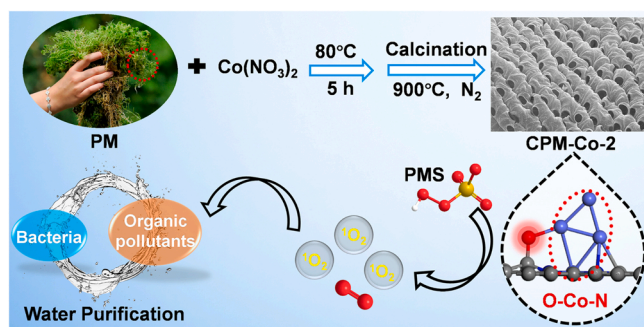
The acquired Raman spectra (Fig. 2j) further confirm the surface structure of the support in CPM-Co-2. The bands at 1315 and 1589 cm^{-1} correspond to the D and G bands of graphitic carbon, respectively. When compared with CPM, the intensity ratio of the D and G bands of CPM-Co-2 increases from 0.97 to 1.49, indicating that the introduction of CoNCs increases the defects in CPM [42]. The Brunauer–Emmett–Teller (BET)

method was used to determine the specific surface area of the material before and after loading CoNCs. PM has a 3D porous structure that connects channels with a high specific surface area [43]. The specific surface area of CPM-Co-2 ($427\text{ m}^2\text{ g}^{-1}$) is significantly higher than that of CPM ($352\text{ m}^2\text{ g}^{-1}$), which is probably related to the microporosity brought by the defects (Fig. 2k) [44].

The valence state of the metal is one of the key factors that determines the catalytic efficiency of PMS activation. Therefore, X-ray photoelectron spectroscopy (XPS) was used to analyze the surface chemical state of CPM-Co-2. As shown in Fig. 3a, the full spectrum XPS of CPM confirms the presence of C 1 s, N 1 s, and O 1 s. The high-resolution C 1 s XPS spectrum of CPM shows peaks at 284.58, 285.08, and 287.48 eV, which correspond to C-C, C-N, and C-O groups, respectively (Fig. S20) [45]. The survey spectra of the CPM-Co-2 sample show the presence of Co, C, N, and O (Figs. 3a and S21). The high-resolution N 1 s peak in CPM-Co-2 has four typical peaks at 399.5, 400.2 eV, 401.5 eV and 402.5 eV, corresponding to the presence of pyridinic N, Co-N, pyrrolic N, and graphitic N, respectively [46,47]. The Co-N and Co-O peaks are observed in the N 1 s and O 1 s spectra of CPM-Co-2, respectively, which indicate the construction of a Co-N, O-dual coordination environment (Fig. 3c and d) [48,49]. It is worth noting that XRD shows that the supported Co exists in the metallic form. However, by valence analysis the XPS spectrum of Co 2p, 799.68/783.78 eV, 798.18/782.18 eV, and 796.88/780.58 eV are assigned to Co^{3+} , Co^{2+} , and Co^0 , respectively (Fig. 3b) [50]. The FWHM and spin orbit splitting energy for Co 2p is 5.09 eV and 14.5 eV, respectively. Since Co^{3+} , Co^{2+} and Co^0 coexist within the Co nanocluster, this indicates that the bonding of Co with the abundant O and N in CPM results in electron transfer and changes in the valence states of Co. Furthermore, the CPM-Co-2 composite generates more surface Co^{2+} and Co^{3+} , which act as the main active centers for PMS activation [51]. Raman spectra and XPS characterization were also performed on other samples (CPM-Co-1, CPM-Co-3 and CPM-Co-4), and it was found that different samples had N, O-double coordination as well as similar degree of defects (Figs. S22 and S23). The above results indicate that ultra-small Co nanoclusters were successfully loaded on CPM and interacted with N and O species to tune the charge distribution of Co.

3.3. Catalytic performance of CPM-Co-2 in AOPs

RhB degradation experiments were performed to explore the catalytic properties of the supported nanocluster materials. A large number of pores are observed connecting the channels together, which increases the specific surface area of the catalyst, improves the interaction of pollutants with the active sites, and allows for the adsorption equilibrium to be reached rapidly (i.e., within 5 min, see Fig. S24). Notably, a high concentration of RhB at 200 mg/L was completely degraded by the CPM-Co-2 catalyst within 90 s with a TOC removal rate of 85% (Fig. 4a). And it also showed excellent reproducibility and high catalytic activity in multiple repeated degradation experiments (Fig. S25). Additionally, the reaction rate constant (k) of CPM-Co-2 is 3.35 min^{-1} , which is higher than those of other related catalytic systems; thus, indicating superior catalytic degradation performance (Figs. S26 and S27). Combined with TEM images (Fig. S28), it is found that the size of cobalt nanoclusters supported by different catalysts is nearly the same, but the dispersion density was different. Notably, CPM-Co-2 showed the highest density of nanoclusters. Evidenced by the ICP-MS characterization, the content of Co in the catalyst showed a volcanic variation with increasing the amount of Co precursors (Fig. 4b). Obviously, with the highest cobalt content and densest Co nanoclusters. Moreover, the changing trend of k is consistent with the concentration of cobalt in the catalyst, which strongly suggests that Co is the active site in this system (Fig. 4b). The influence of pH value and temperature on the catalytic activity of the reaction system was also explored (Fig. S29). Since the catalytic system exhibited excellent activity at 25°C and $\text{pH}=7$, the subsequent experiments were finally conducted at $\text{pH}=7$ and 25°C considering the



Scheme 1. Preparation route of CPM-Co-2 catalyst and schematic illustration of antibacterial and organic pollutants degradation mechanism for water purification.

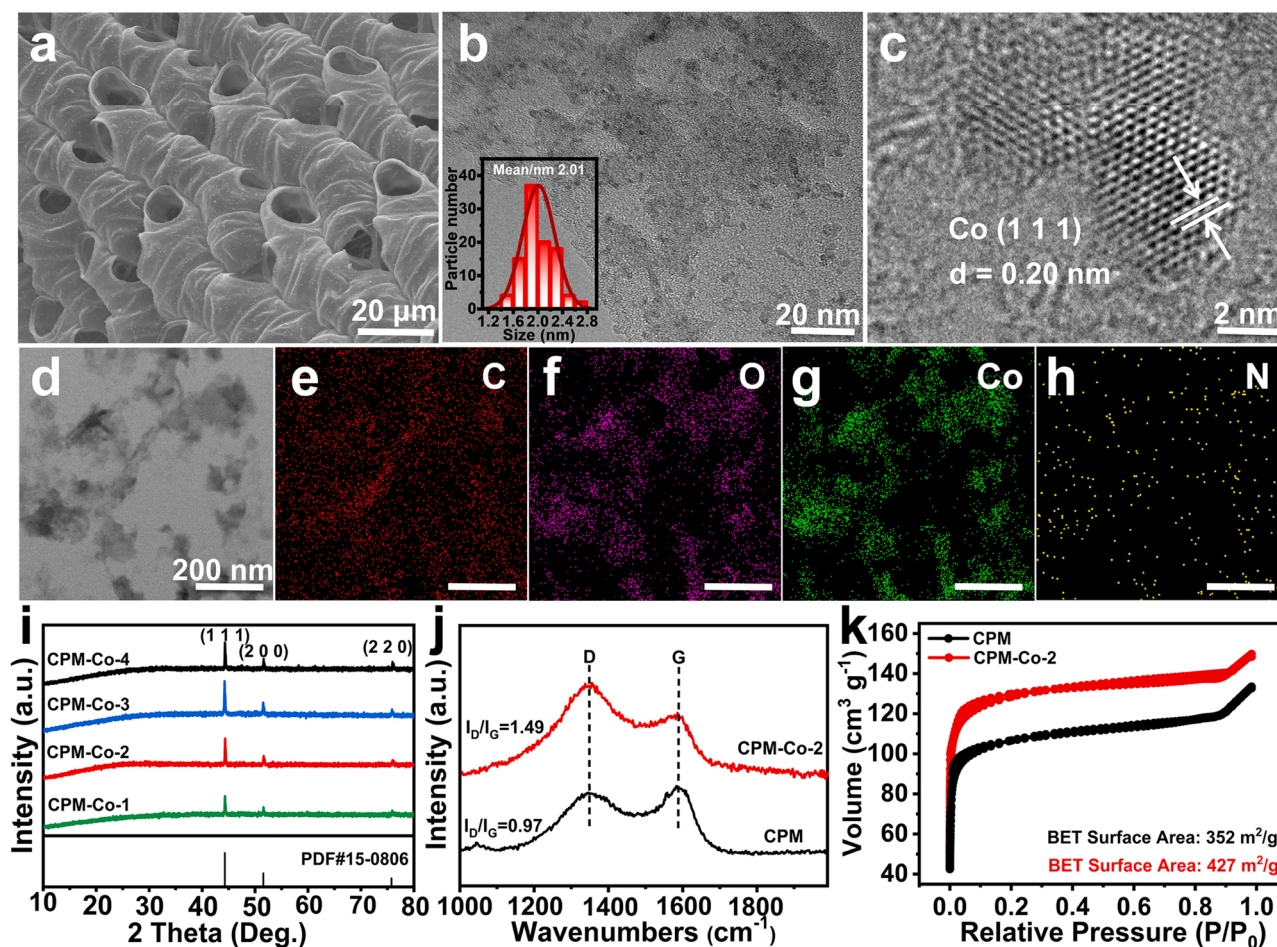


Fig. 2. Structural characterization of the CPM-Co-2. a) SEM image, b) TEM images, c) HRTEM image, d-h) EDX mappings of CPM-Co-2. i) The XRD patterns of different cobalt-based catalysts. j) Raman spectra and k) N_2 adsorption-desorption isotherms of CPM and CPM-Co-2.

practical application requirements and catalytic performance. Subsequently, the influence of inorganic anions on the RhB degradation was also investigated (Fig. S30). The degradation rate of RhB was affected to some extent due to the quenching effect of inorganic anions (chloride ions, carbonate, dihydrogen phosphate) on the active substances produced in the AOPs [52]. CoNCs were used to further verify that the electron delocalization realized through the combination of Co with N and O is the phenomenon affecting the Fenton-like catalytic reaction. As shown in Fig. S31, without introducing CPM in the catalyst, CoNCs exhibits a RhB degradation rate of 7%, indicating that the porous structure of the support helps in effectively dispersing the cobalt clusters and regulating the electron density of Co using N and O. Subsequently, the versatility of CPM-Co-2 was evaluated by degrading other refractory organic pollutants. Complete degradation of BPA and 2,4-DCP is achieved within 5 min, and the TOC removal rates reached 69% and 71%, respectively, demonstrating the versatility of the excellent Fenton-like activity of CPM-Co-2 (Figs. S32 and S33). As shown in Figs. S34–S37, the major intermediates generated during the RhB, 2,4-DCP and BPA degradation were tested by LC-MS. Subsequently, the mineralization rates of RhB, 2,4-DCP and BPA were up to 95%, 93% and 94% after 15 min reaction, respectively, showing low toxicity to the solution. Furthermore, the k -value is used to compare the degradation rates of organic pollutants in the various Fenton-like processes, and the catalyst CPM-Co-2 showed obvious dominant efficiency as high as 116.5, 25.9, and 28.63 $\mu\text{mol s}^{-1} \text{g}^{-1}$ for RhB, BPA, and 2,4-DCP, respectively (Table S1).

3.4. Exploration of active radical species

The active radical species generated in the Fenton-like reaction of the CPM-Co-2/PMS system were determined via radical quenching experiments (Figs. 4c, S38, and S39) [53]. When *tert*-butanol (TBA) or ethanol (EtOH) is added to the reaction mixture, the RhB degradation efficiency decreases slightly, implying that hydroxyl radicals ($\bullet\text{OH}$) and sulfate radicals ($\text{SO}_4^{\bullet-}$) are not the main active species during the reaction. However, the degradation process significantly decreases in the presence of benzoquinone (BQ), which indicates that superoxide radicals ($\text{O}_2^{\bullet-}$) participate in the reaction system. Furthermore, when furfuryl alcohol (FFA) is added, the degradation of RhB is almost completely quenched, suggesting that $^1\text{O}_2$ is the main reactive species during the CPM-Co-2 catalyzed activation of PMS. To further verify the active species in the CPM-Co-2/PMS catalytic system, electron paramagnetic resonance (EPR) experiments were conducted using 2,2,6,6-tetramethylpiperidine (TEMP) as a spin-trapping agent [36]. As displayed in Fig. 4d, CPM-Co-2 or PMS alone generate a weak EPR signal of TEMP^1O_2 . However, when CPM-Co-2 is added together with PMS, the typical triple characteristic signal of 1:1:1 is significantly enhanced. These results clearly confirm that the Fenton-like reaction of the CPM-Co-2 catalyst effectively catalyzes the generation of active $^1\text{O}_2$.

3.5. The PMS-based oxidation mechanism

The PMS-based oxidation mechanism is elaborated in the Supporting Information. As the main active center, Co^{2+} in CPM-Co-2 catalyst preferentially breaks the peroxide bond ($-\text{O}-\text{O}-$) of PMS to generate $\text{SO}_4^{\bullet-}$,

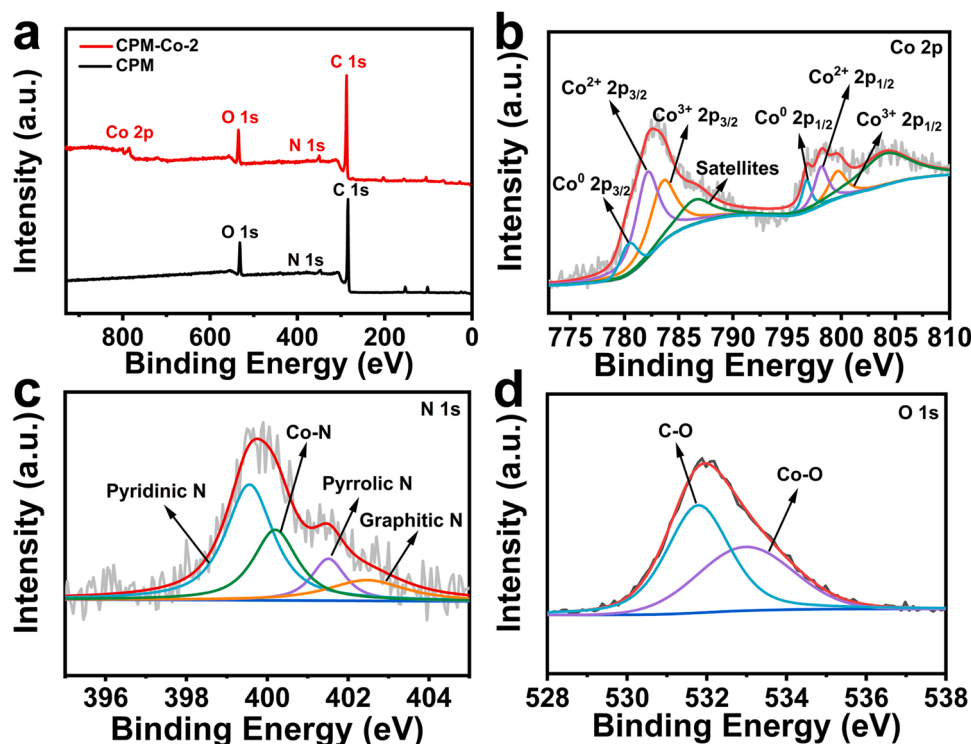


Fig. 3. a) XPS spectrum of CPM and CPM-Co-2. High-resolution XPS spectra of b) Co 2p, c) N 1s, and d) O 1s of CPM-Co-2.

OH^- and Co^{3+} (equation (1)). The resulting $\text{SO}_4^{\bullet-}$ can be converted to $\bullet\text{OH}$ (equation (2)). Co^{3+} and Co^0 can activate PMS to generate Co^{2+} , $\text{SO}_4^{\bullet-}$, and OH^- (equations (3) and (4)). In addition, Co^0 can react with Co^{3+} to form Co^{2+} , ensuring sufficient Co^{2+} to activate PMS (equation (5)). The periodic cycle between $\text{Co}^{2+}/\text{Co}^{3+}$ ions enable the CPM-Co-2/PMS system very effective in catalyzing. HSO_5^- reacts with H_2O to produce H_2O_2 (equation (6)), and further reacts with $\bullet\text{OH}$ to get HO_2^{\bullet} (equation (7)). Subsequently, the decomposition of HO_2^{\bullet} produces $\text{O}_2^{\bullet-}$ (equation (8)). Furthermore, $\text{O}_2^{\bullet-}$ free radicals can react with HO^{\bullet} to form $^1\text{O}_2$ and self-react to form H_2O_2 and $^1\text{O}_2$ (equations (9) and (10)). The continuously generated free radicals can almost completely mineralize RhB to CO_2 and H_2O .

3.6. Magnetic properties of the CPM-Co-2 catalyst

The economic benefits, magnetic properties, and reusability of the catalysts are important parameters for practical applications [54,55]. A magnetic evaluation was conducted, and the saturation magnetization value of CPM-Co-2 is 73.2 emu/g, indicating excellent magnetic properties (Fig. 4e). As shown in the inset of Fig. 4e, CPM-Co-2 can be easily collected in an externally applied magnetic field during solid-liquid separation. As shown in Figs. 4f and S40, the stability of CPM-Co-2 is evaluated over seven consecutive reactions. After the cyclic reactions, CPM-Co-2 could still degrade 97% of the RhB. Additionally, the Co 2p XPS spectrum of CPM-Co-2 after seven cyclic reactions showed a slight reduction of Co^{2+} compared to that before the catalytic reaction (about 9.8%) (Fig. S41 and Table S2). The XRD and TEM characterizations of CPM-Co-2 after seven degradations also showed ignorable changes (Figs. S42 and S43). All of these experimental results indicate that the catalyst has excellent stability. The cobalt ion leaching test was performed, the solution was heated and concentrated to 20 mL after seven cyclic reactions. The results showed that the amount of Co ions detected during the reaction was 0.37 mg/L by ICP-MS, which had a negligible effect on the whole degradation process as well as the water environment. The ultra-small CoNCs, through the O-Co-N sites, are well immobilized on the porous graphitized biocarbon substrate and exhibit

satisfactory durability during catalysis.

3.7. Antibacterial activities of CPM-Co-2 catalyst

To expand the potential application of the CPM-Co-2 catalyst for deep-water purification, the antibacterial activities of CPM-Co-2 against *E. coli* and *S. aureus* were investigated. The antibacterial activity was assessed through colony formation of *E. coli* and *S. aureus* after treatment with different systems, and photographs of representative experimental groups were taken (Fig. 5a–c). When compared with the control group, the number of *E. coli* colonies is not significantly decreased by the addition of PMS or CPM-Co-2, and the survival rates are 85% and 81%, respectively. CPM-Co-2 has mild antibacterial activity also because of its possible physical/mechanical loss to the bacteria when used as a substrate carbon material. Under the combined effect of the CPM-Co-2 catalyst and PMS, bacteria are almost completely killed within 20 min, and the bacterial inhibition rate is nearly 100%, which is obviously better than that of other related catalytic systems. As shown in Fig. S44, PMS alone can decompose and produce free radicals, which have certain bacteriostatic effects on *E. coli*. In the presence of CPM-Co-2, the concentration of PMS decreases by one order of magnitude, with a similar bacterial-killing efficiency. A similar trend is also observed in the antimicrobial tests for *S. aureus*. Therefore, the synergy between CPM-Co-2 and PMS enhances antibacterial activity.

Fluorescence imaging experiments were performed for cell viability assay to further investigate the enhanced antibacterial activity of PMS by CPM-Co-2 (Fig. 5d). Dead bacteria were labeled with PI to show red fluorescence, whereas living bacteria were labeled with STOP 9 to show green fluorescence [56]. The control group shows almost all-green fluorescence, indicating good bacterial activity. Only a few red fluorescent cells are observed in bacteria treated with PMS or CPM-Co-2 alone. When PMS and CPM-Co-2 are added together, red fluorescence dominates, indicating that almost all bacteria are killed owing to the enhanced antibacterial activity of CPM-Co-2/PMS. SEM was used to observe whether the morphology of the *E. coli* and *S. aureus* cells changed after the different treatments. As shown in Fig. 5e, untreated

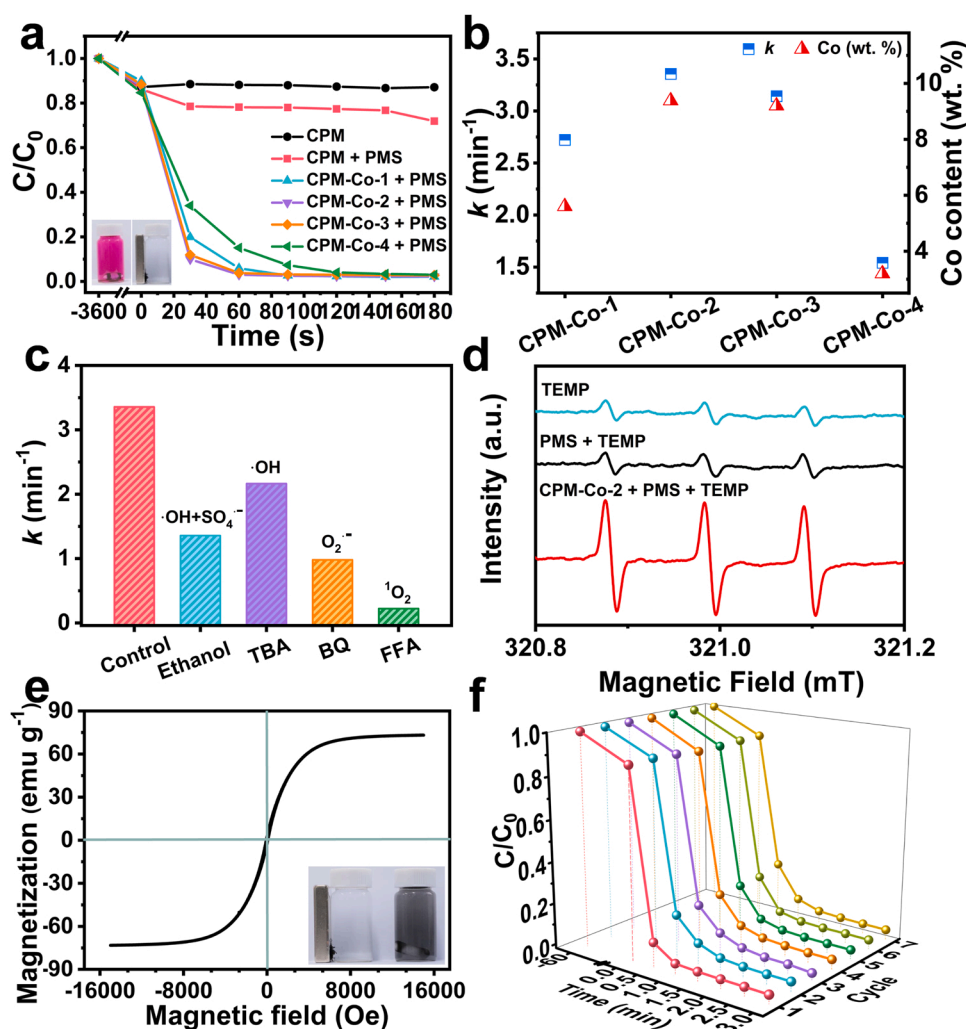


Fig. 4. a) Fenton-Like degradation of RhB by different catalysts. b) The relationship between the reaction rate constants and the contents of Co in different catalysts. c) The change of reaction rate constants under different radical quenching conditions. d) The EPR spectra for the detection of ¹O₂. e) Magnetization behavior of CPM-Co-2. f) The consecutive run to investigate the stability of catalytic activity for CPM-Co-2. Reaction condition: RhB = 200 mg/L, catalyst = 0.2 g/L, PMS = 0.2 g/L, pH = 7 and 25 °C.

E. coli cells are rod-shaped, whereas untreated *S. aureus* cells appear as cocci in the control group. The cell walls of both bacteria are smooth and intact. After PMS or CPM-Co-2 treatment, the *E. coli* cell surface becomes rough and wrinkled and a small part of the bacterial membrane is destroyed. Remarkably, the bacterial cells are severely damaged when exposed to the PMS + CPM-Co-2 system, completely destroying and losing cell integrity. The SEM results for the treated *S. aureus* cells are the same as those of the treated *E. coli* cells. These results are also consistent with those of the spread plate assays.

The involved bactericidal mechanism was investigated via radical quenching in the inactivation experiment of *E. coli*. As shown in Fig. S45, after the addition of TBA or methanol (radical scavenger for $\bullet\text{OH}$ and $\text{SO}_4^{\bullet-}$, respectively), the inhibition rates were 92% and 88%, respectively, which indicates that the presence of active species other than $\bullet\text{OH}$ and $\text{SO}_4^{\bullet-}$ during the inactivation of *E. coli*. However, when FFA, a unique scavenger for ¹O₂ was added, there was almost no variation in *E. coli* colonies, suggesting the crucial role of ¹O₂ in the inactivation experiment of bacteria. The above results indicate that non-free radicals play a leading role in the CPM-Co-2/PMS bactericidal system, wherein ¹O₂ serves as the main reactive oxygen species participating in the reaction [57]. Combined with the above experiments, it was shown that CPM-Co-2 significantly enhances the antibacterial activity of PMS, which could be attributed to the synergy between PMS and CPM-Co-2. On the one hand, the porous nature of CPM helps to expose the abundant active sites on the ultra-small CoNCs. On the other hand, the synergistic effect of N and O helps to regulate the electron density of Co to

fully activate the low concentration of PMS and quickly generate a large amount of ¹O₂. The acquired results also reveal that the CPM-Co-2/PMS system has excellent antibacterial activity against both gram-positive and gram-negative bacteria.

4. Conclusion

In conclusion, the nanocluster catalyst, CPM-Co-2, with highly active novel O-Co-N sites was prepared on a large-scale using biomass-derived carbon that is rich in N- and O-containing functional groups as a support. DFT calculations showed that the introduction of O facilitated the shift of the *d*-band center of O-Co-N away from the Fermi level, decreased the energy barrier for adsorbents, accelerated the rate-limiting step, and greatly increased the generation of ROS. CPM-Co-2 exhibited a higher efficiency than most traditional Fenton-like catalysts, and could robustly degrade POPs and exhibit excellent antibacterial activity in wastewater. Therefore, we anticipate that our proposed N, O-dual coordination regulation system will direct the rational design of highly active catalysts in the future.

CRediT authorship contribution statement

Fangfang Dai: Conceptualization, Methodology, Visualization, Writing – original draft. **Mingsen Xie:** Data curation, Writing – original draft. **Shuoxuan Wang:** Methodology. **Weiqliang Lv:** Methodology, Formal analysis. **Yong Wang:** Formal analysis. **Zhen Zhang:** Writing –

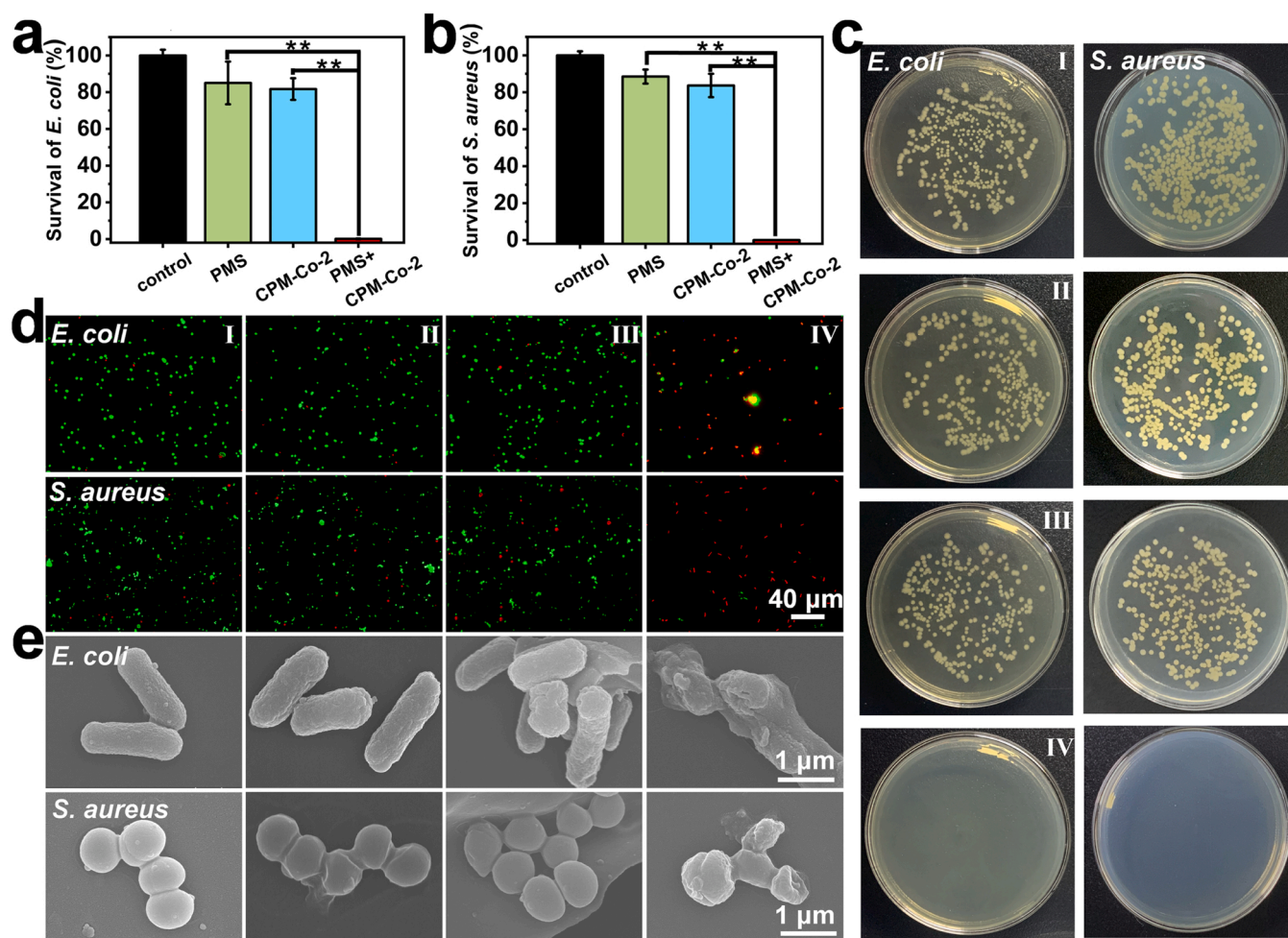


Fig. 5. Survival rates of a) *E. coli* and b) *S. aureus* after different treatments were determined by counting colony formation units. c) The photographs of colony formation assay for *E. coli* (left row) and *S. aureus* (right row) after different treatments. d) Representative fluorescence images of *E. coli* and *S. aureus* after different treatments (green represents live cells, red represents dead cells). e) The SEM images of *E. coli* and *S. aureus* after different treatments. The bacterial cells were treated with PBS (I), PMS (II), CPM-Co-2 (III), and PMS + CPM-Co-2 (IV), respectively. Statistical significance of each group was carried out three times in parallel. Student's *t*-test was used to calculate: **p* < 0.05, ***p* < 0.01, ****p* < 0.001.

review & editing. **Xiaoquan Lu:** Conceptualization, Writing – review & editing, Project administration, Supervision, Funding acquisition.

Declaration of Competing Interest

The authors declare that they have no known competing financial interests or personal relationships that could have appeared to influence the work reported in this paper.

Data availability

Data will be made available on request.

Acknowledgments

This work was supported by the National Natural Science Foundation of China (Nos. 22174110, 22127803, 21705117); Program of Tianjin Science and Technology Major Project and Engineering (19ZXYSY00090); the Industrial Support Plan of Gansu Provincial Department of Education (2021cyzc-01); the Special Fund Project for Guiding Local Scientific and Technological Development by the Central Government (No. 2020-2060503-17).

Appendix A. Supplementary material

Supplementary data associated with this article can be found in the online version at [doi:10.1016/j.apcatb.2023.122510](https://doi.org/10.1016/j.apcatb.2023.122510).

References

- [1] R. Song, H. Chi, Q. Ma, D. Li, X. Wang, W. Gao, H. Wang, X. Wang, Z. Li, C. Li, Highly efficient degradation of persistent pollutants with 3D nanocone TiO₂-based photoelectrocatalysis, *J. Am. Chem. Soc.* 143 (2021) 13664–13674, <https://doi.org/10.1021/jacs.1c05008>.
- [2] L. Yang, H. Yang, S. Yin, X. Wang, M. Xu, G. Lu, Z. Liu, H. Sun, Fe single-atom catalyst for efficient and rapid Fenton-like degradation of organics and disinfection against bacteria, *Small* 18 (2022) 2104941, <https://doi.org/10.1002/sml.202104941>.
- [3] Y. Wang, H. Cao, C. Chen, Y. Xie, H. Sun, X. Duan, S. Wang, Metal-free catalytic ozonation on surface-engineered graphene: microwave reduction and heteroatom doping, *Chem. Eng. J.* 355 (2019) 118–129, <https://doi.org/10.1016/j.cej.2018.08.134>.
- [4] R. Zhang, Y. Liu, M. He, Y. Su, X. Zhao, M. Elimelech, Z. Jiang, Antifouling membranes for sustainable water purification: strategies and mechanisms, *Chem. Soc. Rev.* 45 (2016) 5888–5924, <https://doi.org/10.1039/c5cs00579e>.
- [5] T. Skorjanc, D. Shetty, A. Trabolsi, Pollutant removal with organic macrocycle-based covalent organic polymers and frameworks, *Chem* 7 (2021) 882–918, <https://doi.org/10.1016/j.chempr.2021.01.002>.
- [6] S. Xie, S. Wu, S. Bao, Y. Wang, Y. Zheng, D. Deng, L. Huang, L. Zhang, M. Lee, Z. Huang, Intelligent mesoporous materials for selective adsorption and mechanical release of organic pollutants from water, *Adv. Mater.* 30 (2018) 1800683, <https://doi.org/10.1002/adma.201800683>.

- [7] W. Xiang, R. Qu, X. Wang, Z. Wang, M. Bin-Jumah, A.A. Allam, F. Zhu, Z. Huo, Removal of 4-chlorophenol, bisphenol A and nonylphenol mixtures by aqueous chlorination and formation of coupling products, *Chem. Eng. J.* 402 (2020), 126140, <https://doi.org/10.1016/j.cej.2020.126140>.
- [8] Y. Gao, J. Jiang, Y. Zhou, S.Y. Pang, J. Ma, C. Jiang, Y. Yang, Z.S. Huang, J. Gu, Q. Guo, J.B. Duan, J. Li, Chlorination of bisphenol S: kinetics, products, and effect of humic acid, *Water Res.* 131 (2018) 208–217, <https://doi.org/10.1016/j.watres.2017.12.049>.
- [9] S. Lim, J.L. Shi, U. von Gunten, D.L. McCurry, Ozonation of organic compounds in water and wastewater: a critical review, *Water Res.* 213 (2022), 118053, <https://doi.org/10.1016/j.watres.2022.118053>.
- [10] S.-M. Hao, J. Qu, Z.-S. Zhu, X.-Y. Zhang, Q.-Q. Wang, Z.-Z. Yu, Hollow manganese silicate nanotubes with tunable secondary nanostructures as excellent fenton-type catalysts for dye decomposition at ambient temperature, *Adv. Funct. Mater.* 26 (2016) 7334–7342, <https://doi.org/10.1002/adfm.201603315>.
- [11] S. An, G. Zhang, T. Wang, W. Zhang, K. Li, C. Song, J.T. Miller, S. Miao, J. Wang, X. Guo, High-Density ultra-small clusters and single-atom Fe sites embedded in graphitic carbon nitride (g-C₃N₄) for highly efficient catalytic advanced oxidation processes, *ACS Nano* 12 (2018) 9441–9450, <https://doi.org/10.1021/acsnano.8b04693>.
- [12] M. Xing, W. Xu, C. Dong, Y. Bai, J. Zeng, Y. Zhou, J. Zhang, Y. Yin, Metal sulfides as excellent co-catalysts for H₂O₂ decomposition in advanced oxidation processes, *Chem* 4 (2018) 1359–1372, <https://doi.org/10.1016/j.chempr.2018.03.002>.
- [13] M. Xie, F. Dai, Y. Wang, W. Lv, Z. Zhang, X. Lu, Electronic metal-support interaction directing the design of Fe(III)-based catalysts for efficient advanced oxidation processes by dual reaction paths, *Small* (2022) 2203269, <https://doi.org/10.1002/smll.202203269>.
- [14] X. Zhang, B. Xu, S. Wang, X. Li, C. Wang, B. Liu, F. Han, Y. Xu, P. Yu, Y. Sun, Tetracycline degradation by peroxymonosulfate activated with CoN_x active sites: performance and activation mechanism, *Chem. Eng. J.* 431 (2022), 133477, <https://doi.org/10.1016/j.cej.2021.133477>.
- [15] K. Cao, T. Zoberbier, J. Biskupek, A. Botos, R.L. McSweeney, A. Kurtoglu, C. T. Stoppello, A.V. Markevich, E. Besley, T.W. Chamberlain, U. Kaiser, A. N. Khlbystov, Comparison of atomic scale dynamics for the middle and late transition metal nanocatalysts, *Nat. Commun.* 9 (2018) 3382, <https://doi.org/10.1038/s41467-018-05831-z>.
- [16] B. Liu, Q. Zhang, Z. Jin, L. Zhang, L. Li, Z. Gao, C. Wang, H. Xie, Z. Su, Uniform pomegranate-like nanoclusters organized by ultrafine transition metal oxide@nitrogen-doped carbon subunits with enhanced lithium storage properties, *Adv. Energy Mater.* 8 (2018) 1702347, <https://doi.org/10.1002/aenm.201702347>.
- [17] J.P. Wilcoxon, B.L. Abrams, Synthesis, structure and properties of metal nanoclusters, *Chem. Soc. Rev.* 35 (2006) 1162–1194, <https://doi.org/10.1039/b517312b>.
- [18] T. Ishida, T. Murayama, A. Taketoshi, M. Haruta, Importance of size and contact structure of gold nanoparticles for the genesis of unique catalytic processes, *Chem. Rev.* 120 (2020) 464–525, <https://doi.org/10.1021/acs.chemrev.9b00551>.
- [19] J. Deng, H. Li, J. Xiao, Y. Tu, D. Deng, H. Yang, H. Tian, J. Li, P. Ren, X. Bao, Triggering the electrocatalytic hydrogen evolution activity of the inert two-dimensional MoS₂ surface via single-atom metal doping, *Energy Environ. Sci.* 8 (2015) 1594–1601, <https://doi.org/10.1039/c5ee00751h>.
- [20] E. Jung, H. Shin, B.H. Lee, V. Efremov, S. Lee, H.S. Lee, J. Kim, W. Hooch Antink, S. Park, K.S. Lee, S.P. Cho, J.S. Yoo, Y.E. Sung, T. Hyeon, Atomic-level tuning of Co-N-C catalyst for high-performance electrochemical H₂O₂ production, *Nat. Mater.* 19 (2020) 436–442, <https://doi.org/10.1038/s41563-019-0571-5>.
- [21] Y. Qin, G. Li, Y. Gao, L. Zhang, Y.S. Ok, T. An, Persistent free radicals in carbon-based materials on transformation of refractory organic contaminants (ROCs) in water: a critical review, *Water Res.* 137 (2018) 130–143, <https://doi.org/10.1016/j.watres.2018.03.012>.
- [22] L. Wang, M.X. Chen, Q.Q. Yan, S.L. Xu, S.Q. Chu, P. Chen, Y. Lin, H.W. Liang, A sulfur-tethering synthesis strategy toward high-loading atomically dispersed noble metal catalysts, *Sci. Adv.* 5 (2019) eaax6322, <https://doi.org/10.1126/sciadv.aax6322>.
- [23] Z. Wang, E. Almatrafi, H. Wang, H. Qin, W. Wang, L. Du, S. Chen, G. Zeng, P. Xu, Cobalt single atoms anchored on oxygen-doped tubular carbon nitride for efficient peroxymonosulfate activation: simultaneous coordination structure and morphology modulation, *Angew. Chem. Int. Ed.* 61 (2022), e202202338, <https://doi.org/10.1002/anie.202202338>.
- [24] Y. Cheng, S. Zhao, B. Johannessen, J.P. Veder, M. Saunders, M.R. Rowles, M. Cheng, C. Liu, M.F. Chisholm, R. De Marco, H.M. Cheng, S.Z. Yang, S.P. Jiang, Atomically dispersed transition metals on carbon nanotubes with ultrahigh loading for selective electrochemical carbon dioxide reduction, *Adv. Mater.* 30 (2018) 1706287, <https://doi.org/10.1002/adma.201706287>.
- [25] T. Lu, T. Li, D. Shi, J. Sun, H. Pang, L. Xu, J. Yang, Y. Tang, In situ establishment of Co/MoS₂ heterostructures onto inverse opal-structured N,S-doped carbon hollow nanospheres: Interfacial and architectural dual engineering for efficient hydrogen evolution reaction, *SmartMat* 2 (2021) 591–602, <https://doi.org/10.1002/smm2.1063>.
- [26] H. Jin, P. Li, P. Cui, J. Shi, W. Zhou, X. Yu, W. Song, C. Cao, Unprecedentedly high activity and selectivity for hydrogenation of nitroarenes with single atomic Co₁N₃P₁ sites, *Nat. Commun.* 13 (2022) 723, <https://doi.org/10.1038/s41467-022-28367-9>.
- [27] X. Li, X. Huang, S. Xi, S. Miao, J. Ding, W. Cai, S. Liu, X. Yang, H. Yang, J. Gao, J. Wang, Y. Huang, T. Zhang, B. Liu, Single cobalt atoms anchored on porous N-doped graphene with dual reaction sites for efficient Fenton-like catalysis, *J. Am. Chem. Soc.* 140 (2018) 12469–12475, <https://doi.org/10.1021/jacs.8b05992>.
- [28] S. Zhang, M. Jin, T. Shi, M. Han, Q. Sun, Y. Lin, Z. Ding, L.R. Zheng, G. Wang, Y. Zhang, H. Zhang, H. Zhao, Electrocatalytically active Fe-(O-C₂)₄ single-atom sites for efficient reduction of nitrogen to ammonia, *Angew. Chem. Int. Ed.* 59 (2020) 13423–13429, <https://doi.org/10.1002/anie.202005930>.
- [29] B.C. Hodges, E.L. Cates, J.H. Kim, Challenges and prospects of advanced oxidation water treatment processes using catalytic nanomaterials, *Nat. Nanotechnol.* 13 (2018) 642–650, <https://doi.org/10.1038/s41565-018-0216-x>.
- [30] Y. Chen, G. Zhang, H. Liu, J. Qu, Confining free radicals in close vicinity to contaminants enables ultrafast Fenton-like processes in the interspersing of MoS₂ membranes, *Angew. Chem. Int. Ed.* 58 (2019) 8134–8138, <https://doi.org/10.1002/anie.201903531>.
- [31] C. Wang, J. Kim, J. Tang, J. Na, Y.M. Kang, M. Kim, H. Lim, Y. Bando, J. Li, Y. Yamauchi, Large-scale synthesis of MOF-derived superporous carbon aerogels with extraordinary adsorption capacity for organic solvents, *Angew. Chem. Int. Ed.* 59 (2020) 2066–2070, <https://doi.org/10.1002/anie.201913719>.
- [32] P.V. Nidheesh, A. Gopinath, N. Ranjith, A. Praveen Akre, V. Sreedharan, M. Suresh Kumar, Potential role of biochar in advanced oxidation processes: a sustainable approach, *Chem. Eng. J.* 405 (2021), 126582, <https://doi.org/10.1016/j.cej.2020.126582>.
- [33] Y. Zhu, W. Sun, W. Chen, T. Cao, Y. Xiong, J. Luo, J. Dong, L. Zheng, J. Zhang, X. Wang, C. Chen, Q. Peng, D. Wang, Y. Li, Scale-up biomass pathway to cobalt single-site catalysts anchored on N-doped porous carbon nanobelt with ultrahigh surface area, *Adv. Funct. Mater.* 28 (2018) 1802167, <https://doi.org/10.1002/adfm.201802167>.
- [34] L. Zhou, P. Fu, D. Wen, Y. Yuan, S. Zhou, Self-constructed carbon nanoparticles-coated porous biocarbon from plant moss as advanced oxygen reduction catalysts, *Appl. Catal. B Environ.* 181 (2016) 635–643, <https://doi.org/10.1016/j.apcatb.2015.08.035>.
- [35] X. He, N. Zheng, R. Hu, Z. Hu, J.C. Yu, Hydrothermal and pyrolytic conversion of biomasses into catalysts for advanced oxidation treatments, *Adv. Funct. Mater.* 31 (2020) 2006505, <https://doi.org/10.1002/adfm.202006505>.
- [36] X. Mi, P. Wang, S. Xu, L. Su, H. Zhong, H. Wang, Y. Li, S. Zhan, Almost 100% peroxymonosulfate conversion to singlet oxygen on single-atom CoN₂₊₂ sites, *Angew. Chem. Int. Ed.* 60 (2021) 4588–4593, <https://doi.org/10.1002/anie.202014472>.
- [37] Y. Shang, X. Xu, B. Gao, S. Wang, X. Duan, Single-atom catalysis in advanced oxidation processes for environmental remediation, *Chem. Soc. Rev.* 50 (2021) 5281–5322, <https://doi.org/10.1039/d0cs01032d>.
- [38] M. Xie, F. Dai, J. Li, X. Dang, J. Guo, W. Lv, Z. Zhang, X. Lu, Tailoring the electronic metal-support interactions in supported atomically dispersed gold catalysts for efficient Fenton-like reaction, *Angew. Chem. Int. Ed.* 60 (2021) 14370–14375, <https://doi.org/10.1002/anie.202103652>.
- [39] C. Song, Q. Zhan, F. Liu, C. Wang, H. Li, X. Wang, X. Guo, Y. Cheng, W. Sun, L. Wang, J. Qian, B. Pan, Overturned loading of inert CeO₂ to active Co₃O₄ for unusually improved catalytic activity in Fenton-like reactions, *Angew. Chem. Int. Ed.* 61 (2022), e202200406, <https://doi.org/10.1002/anie.202200406>.
- [40] C. Wu, D. Liu, H. Li, J. Li, Molybdenum carbide-decorated metallic cobalt@nitrogen-doped carbon polyhedrons for enhanced electrocatalytic hydrogen evolution, *Small* 14 (2018) 1704227, <https://doi.org/10.1002/smll.201704227>.
- [41] G. Wan, C. Yang, W. Zhao, Q. Li, N. Wang, T. Li, H. Zhou, H. Chen, J. Shi, Anion-regulated selective generation of cobalt sites in carbon: toward superior bifunctional electrocatalysis, *Adv. Mater.* 29 (2017) 1703436, <https://doi.org/10.1002/adma.201703436>.
- [42] F. Li, T. Qin, Y. Sun, R. Jiang, J. Yuan, X. Liu, A.P. O'Mullane, Preparation of a one-dimensional hierarchical MnO@CNT@Co-N/C ternary nanostructure as a high-performance bifunctional electrocatalyst for rechargeable Zn-air batteries, *J. Mater. Chem. A* 9 (2021) 22533–22543, <https://doi.org/10.1039/d1ta07259e>.
- [43] F. Dai, M. Xie, Y. Wang, L. Zhang, Z. Zhang, X. Lu, Synergistic effect improves the response of active sites to target variations for picomolar detection of silver ions, *Anal. Chem.* 94 (2022) 10462–10469, <https://doi.org/10.1021/acs.analchem.2c01665>.
- [44] B. Zhang, M. Le, J. Chen, H. Guo, J. Wu, L. Wang, Enhancing defects of N-doped carbon nanospheres via ultralow Co atom loading engineering for a high-efficiency oxygen reduction reaction, *ACS Appl. Energy Mater.* 4 (2021) 3439–3447, <https://doi.org/10.1021/acsaem.0c03197>.
- [45] S. He, J. Huang, Q. Zhang, W. Zhao, Z. Xu, W. Zhang, Bamboo-like nanozyme based on nitrogen-doped carbon nanotubes encapsulating cobalt nanoparticles for wound antibacterial applications, *Adv. Funct. Mater.* 31 (2021) 2105198, <https://doi.org/10.1002/adfm.202105198>.
- [46] C. Zhang, L. Fu, N. Liu, M. Liu, Y. Wang, Z. Liu, Synthesis of nitrogen-doped graphene using embedded carbon and nitrogen sources, *Adv. Mater.* 23 (2011) 1020–1024, <https://doi.org/10.1002/adma.201004110>.
- [47] P. Yu, L. Wang, F. Sun, Y. Xie, X. Liu, J. Ma, X. Wang, C. Tian, J. Li, H. Fu, Co nanodisks rooted on Co-N-C nanosheets as efficient oxygen electrocatalyst for Zn-air batteries, *Adv. Mater.* 31 (2019), e1901666, <https://doi.org/10.1002/adma.201901666>.
- [48] Z. Chen, Y. Ha, H. Jia, X. Yan, M. Chen, M. Liu, R. Wu, Oriented transformation of Co-LDH into 2D/3D ZIF-67 to achieve Co-N-C hybrids for efficient overall water splitting, *Adv. Energy Mater.* 9 (2019) 1803918, <https://doi.org/10.1002/aenm.201803918>.
- [49] K. Wang, G. Gu, S. Hu, J. Zhang, X. Sun, F. Wang, P. Li, Y. Zhao, Z. Fan, X. Zou, Molten salt assistant synthesis of three-dimensional cobalt doped graphitic carbon nitride for photocatalytic N₂ fixation: experiment and DFT simulation analysis, *Chem. Eng. J.* 368 (2019) 896–904, <https://doi.org/10.1016/j.cej.2019.03.037>.
- [50] Y. Long, J. Dai, S. Zhao, Y. Su, Z. Wang, Z. Zhang, Atomically dispersed cobalt sites on graphene as efficient periodate activators for selective organic pollutant

- degradation, *Environ. Sci. Technol.* 55 (2021) 5357–5370, <https://doi.org/10.1021/acs.est.0c07794>.
- [51] Q. Yang, H. Choi, D.D. Dionysiou, Nanocrystalline cobalt oxide immobilized on titanium dioxide nanoparticles for the heterogeneous activation of peroxymonosulfate, *Appl. Catal. B Environ.* 74 (2007) 170–178, <https://doi.org/10.1016/j.apcatb.2007.02.001>.
- [52] C. Chen, T. Ma, Y. Shang, B. Gao, B. Jin, H. Dan, Q. Li, Q. Yue, Y. Li, Y. Wang, X. Xu, In-situ pyrolysis of Enteromorpha as carbocatalyst for catalytic removal of organic contaminants: considering the intrinsic N/Fe in Enteromorpha and non-radical reaction, *Appl. Catal. B Environ.* 250 (2019) 382–395, <https://doi.org/10.1016/j.apcatb.2019.03.048>.
- [53] X. Duan, J. Kang, W. Tian, H. Zhang, S.-H. Ho, Y.-A. Zhu, Z. Ao, H. Sun, S. Wang, Interfacial-engineered cobalt@carbon hybrids for synergistically boosted evolution of sulfate radicals toward green oxidation, *Appl. Catal. B Environ.* 256 (2019), 117795, <https://doi.org/10.1016/j.apcatb.2019.117795>.
- [54] P. Fang, W. Xia, Y. Zhou, Z. Ai, W. Yin, M. Xia, J. Yu, R.-A. Chi, Q. Yue, Ion-imprinted mesoporous silica/magnetic graphene oxide composites functionalized with Schiff-base for selective Cu(II) capture and simultaneously being transformed as a robust heterogeneous catalyst, *Chem. Eng. J.* 385 (2020), 123847, <https://doi.org/10.1016/j.cej.2019.123847>.
- [55] I. Othman, J. Hisham Zain, M. Abu Haija, F. Banat, Catalytic activation of peroxymonosulfate using CeVO4 for phenol degradation: an insight into the reaction pathway, *Appl. Catal. B Environ.* 266 (2020), 118601, <https://doi.org/10.1016/j.apcatb.2020.118601>.
- [56] S.L. Chua, J.K. Yam, P. Hao, S.S. Adav, M.M. Salido, Y. Liu, M. Givskov, S.K. Sze, T. Tolker-Nielsen, L. Yang, Selective labelling and eradication of antibiotic-tolerant bacterial populations in *Pseudomonas aeruginosa* biofilms, *Nat. Commun.* 7 (2016) 10750, <https://doi.org/10.1038/ncomms10750>.
- [57] X. Zhou, Z. Yang, Y. Chen, H. Feng, J. Yu, J. Tang, X. Ren, J. Tang, J. Wang, L. Tang, Single-atom Ru loaded on layered double hydroxide catalyzes peroxymonosulfate for effective *E. coli* inactivation via a non-radical pathway: efficiency and mechanism, *J. Hazard. Mater.* 440 (2022), 129720, <https://doi.org/10.1016/j.jhazmat.2022.129720>.